

# Attitude Estimation for Space Targets by Exploiting the Quadratic Phase Coefficients of Inverse Synthetic Aperture Radar Imagery

Yejian Zhou<sup>ID</sup>, Lei Zhang<sup>ID</sup>, and Yunhe Cao

**Abstract**—This paper proposes a novel approach to interpreting the satellite attitude based on inverse synthetic aperture radar (ISAR) images. In the conventional viewpoint, quadratic and higher order phase terms of ISAR imagery are regarded as negative factors causing the defocusing phenomenon. In this paper, we introduce how to apply quadratic phase coefficients to estimate target attitude from the ISAR imagery. A geometric projection model of ISAR imaging is built according to radar line of sight, and an explicit expression is also derived to connect target attitude parameters and the image defocusing property. With the accommodation of Broyden–Fletcher–Goldfarb–Shanno algorithm, spatial-variant quadratic phase coefficients together with attitude parameters are determined by an image contrast maximization. We also extend the proposed algorithm to multistatic ISAR applications, where the quadratic phase information lying in simultaneous multistatic ISAR images can be mined to enhance the performance of target attitude estimation. Experimental results illustrate the feasibility of the proposed algorithm.

**Index Terms**—Attitude estimation, image refocusing, imaging geometry analysis, inverse synthetic aperture radar (ISAR) imaging, multistatic ISAR.

## I. INTRODUCTION

AS AN increasing number of satellites are launched on orbit, state analysis of space targets plays an essential role in the space applications, such as monitoring their health state, salvaging a faulty satellite, and warning the crash of uncontrolled space targets [1], [2]. An important aspect of state analysis is the effective determination of the target attitude, which directly represents its operational and potential

Manuscript received May 21, 2018; revised September 17, 2018 and November 9, 2018; accepted December 16, 2018. Date of publication January 15, 2019; date of current version May 28, 2019. This work was supported in part by the National Natural Sciences Foundation of China under Grant 61771372 and Grant 61771367, in part by the National Outstanding Youth Science Fund Project under Grant 61525105, and in part by the National Science Foundation of Shanghai under Grant 1428700. (*Corresponding author: Lei Zhang*.)

Y. Zhou and Y. Cao are with the National Laboratory of Radar Signal Processing, Collaborative Innovation Center of Information Sensing and Understanding, Xidian University, Xi'an 710071, China.

L. Zhang is with the National Laboratory of Radar Signal Processing, Collaborative Innovation Center of Information Sensing and Understanding, Xidian University, Xi'an 710071, China, and also with the School of Electronics and Communication Engineering, Sun Yat-sen University, Guangzhou 510275, China (e-mail: leizhang@xidian.edu.cn).

Color versions of one or more of the figures in this paper are available online at <http://ieeexplore.ieee.org>.

Digital Object Identifier 10.1109/TGRS.2018.2888631

state [3]–[6]. Thanks to the robust working capability, high-resolution radar sensors, like tracking and imaging radar, are generally adopted to accomplish those tasks. The 3-D geometric attitude information of space targets can be retrieved via interpreting high-resolution radar images together with other physical or motion characteristics [7]–[13].

Reviewing the relevant literature [10]–[17], the successful application of most existing methods relies on sufficient radar observation resource [i.e., strictly long-time observation obtaining a sequence of inverse synthetic aperture radar (ISAR) imagery]. However, these methods are limited in use due to different premises which are difficult to meet in many practical circumstances. For example, some typical target characteristics, like the radar cross section, are measured and matched with preexisting simulation data to determine target attitude parameters [11], [12]. This method relies on the preexisting simulation data, which means that it needs to establish a complete full-view simulation database with electronic magnetic computation techniques. Nevertheless, this approach cannot readily retrieve the attitude of unknown targets. Another typical approach is adapting singular value decomposition to reconstruct target scattering points from a multiview ISAR image sequence [14]–[17]. Besides the long-time observation requirement, the major defect of this approach is that the feature association of multiview images is never an easy task in practice, especially when the angular glint phenomenon occurs.

In most existing space target attitude determination approaches, only the magnitude of multiview ISAR images is applied, while the phase of complex-valued ISAR images, as an informative observation resource, is scarcely explored. In this paper, a novel attitude estimation for satellite targets is proposed based on the quadratic phase information of ISAR imagery. First of all, combined with the geometric projection theory [34], it develops a signal model of the scattering point defocusing distribution in ISAR imagery. Based on this, an explicit expression is derived to connect the quadratic phase terms of range-Doppler (RD) images and the target absolute attitude. Then, according to instantaneous radar line-of-sight (LOS) parameters [18], [19], the target attitude is solved with an image contrast maximization for the spatial-variant quadratic phase coefficients. This algorithm can be regarded as a significant extension of ISAR phase adjustment approaches [20]–[23]. It is worth noting that both the

target prior knowledge about the plane component and critical trajectory information (LOS parameters) are utilized in the attitude determination. Experiments demonstrate the feasibility of the proposed algorithm, and a multistatic application is also extended to improve the performance of the target attitude estimation. The main contributions of the proposed algorithm are listed as follows.

- 1) Quadratic phase terms are usually compensated within the phase adjustment for the sake of improving the focal performance of ISAR imagery. They are conventionally treated as phase errors instead of informative elements for the target state interpretation. To the best of our knowledge, it is the first time that the quadratic phase terms have been developed for space target attitude estimation. We believe this paper will provide a new perspective of ISAR image application on the interpretation of space targets.
- 2) Short observation duration requirement is considered as an important advantage over current approaches. Reviewing previous works [10]–[17], [33], almost all current approaches rely on a long-time observation to acquire a target characteristic sequence (i.e., an image sequence). Long-time observation requirements would involve some constraints in practical applications where radar time resource is not sufficient. On the other hand, leveraging the bridge between the image defocusing performance and target attitude parameters, a single ISAR image would be adequate to determine the target attitude with the proposed approach.
- 3) Another contribution is to effectively use radar LOS angles from the satellite track data. The proposed algorithm proves a pivotal way to establish a deterministic motion and geometry model of space target ISAR imaging with radar LOS angles. The work reveals that full utilization of track information is crucial for the deep interpretation of space target radar images.

The remainder of this paper is organized as follows. Section II investigates the geometric model for satellite observation by ISAR while Section III derives an explicit expression of the connection between the defocusing phenomenon and the attitude information of satellite targets. In Section IV, target attitude parameters are retrieved by solving an image contrast maximization, which explores the spatial-variant quadratic phase coefficients. In Section V, the feasibility and accuracy of the proposed algorithm are assessed by simulation experiments. Some conclusions are drawn in Section VI.

## II. OBSERVATION GEOMETRIC PARAMETERS DETERMINATION

It should be emphasized that the proposed method is developed based on the assumption that the flying satellite is under attitude control to maintain three-axis steady attitude in the target Cartesian coordinate system, as is depicted in Fig. 1(b). Most low earth orbit (LEO) satellites are in the Kepler circle orbits, and the geometric definition of the target Cartesian coordinate system is as follows: the  $x$ -axis points to Earth's core, the  $y$ -axis is tangent to the target orbit, which keeps in touch with the target trajectory, and the  $z$ -axis can be

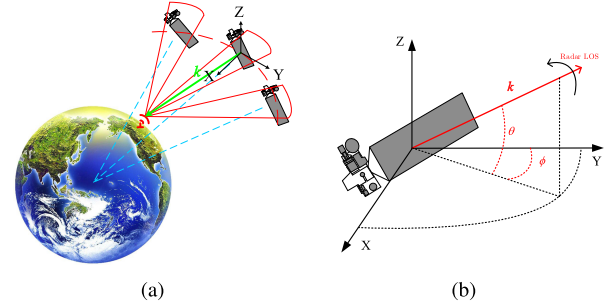


Fig. 1. Satellite target observation geometry. (a) Target observation geometry in 3-D world space. (b) Target observation geometry in the target Cartesian coordinate system.

considered as the normal vector of the target trajectory plane as shown in Fig. 1(a). During the ISAR observation, the satellite target coordinates are invariant in these axes, and the 3-D rotation of the target relative to the ground-based radar is replaced by the time-varying LOS parameters. In this way, the ISAR observation geometry is described with the classical turn-table model, as depicted in Fig. 1(b). Then, two angle parameters are defined to determine the unit LOS direction vector  $\vec{k}$  as follows:

$$\vec{k} = (\cos \theta(t_m) \sin \phi(t_m), \cos \theta(t_m) \cos \phi(t_m), \sin \theta(t_m))^T \quad (1)$$

where  $t_m$  denotes the slow-time relative to the sampling in the azimuth direction, the elevation angle  $\theta(t_m)$  is the intersection angle between the instantaneous radar LOS vector and the  $XOY$  plane, and the azimuth angle  $\phi(t_m)$  is the intersection angle between the  $y$ -axis and the projection of the instantaneous radar LOS vector in the  $XOY$  plane, as shown in Fig. 1(b).

In practical applications, LOS parameter sequences can be obtained by various methods, and here, we provide several methods for reference.

- 1) Solve satellite target two-line orbital element (TLE) ephemeris to determine its position in the SGP4 model. Then, calculate its position relative to the radar station in the SGP4 model [18], [19].
- 2) Solve satellite target orbital elements to determine its position in the earth-centered, earth-fixed (ECEF) coordinate system. After that, calculate its position relative to a radar station in the ECEF coordinate system [24]–[26].
- 3) Explore the azimuth, pitch, and distance parameters from the radar tracking system, and make the atmospheric refraction modification.

In our approach, LOS parameters are obtained by the first method. The validity of the calculated results is confirmed by comparing them with Satellite Tool Kit (STK) simulations and real radar tracking measurements. The comparison of the target subsatellite position between the calculated results and the STK simulation is depicted in Fig. 2 under the longitude latitude altitude coordinate system while the comparison of target observation parameters between the calculated results

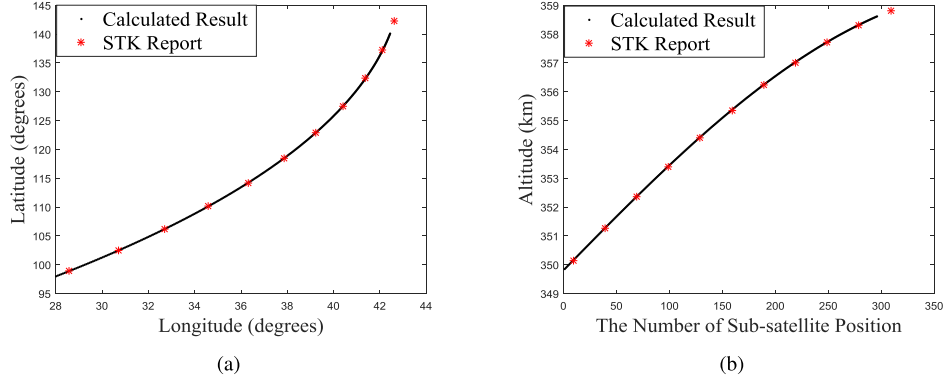


Fig. 2. Comparison of the target subsatellite position between the calculated result and the STK simulation. (a) Comparison of the target longitude and latitude. (b) Comparison of the target altitude.

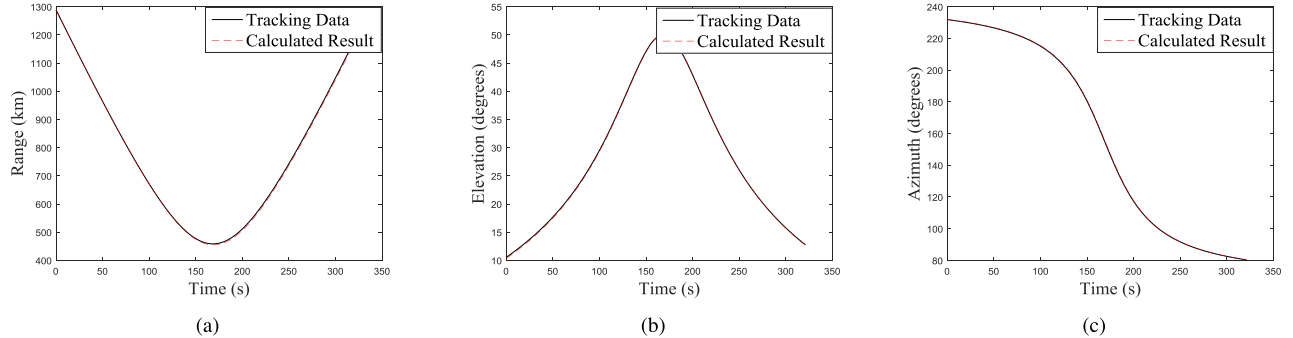


Fig. 3. Comparison of the observation parameters between the calculated result and the measurement. (a) Comparison of the observation range. (b) Comparison of the elevation angle. (c) Comparison of the azimuth angle.

and the measurement is shown in Fig. 3. It confirms the feasibility of the calculation method adopted in this paper, and LOS parameters are deemed to *a priori* in Sections III–V.

### III. SIGNAL MODEL

In this section, an explicit expression is derived to bridge the RD image with the target attitude. Based on the phase analysis of a typical plane component mounted on the target, the RD mapping expression paves a way to interpret satellite attitude from RD imagery. As stated in Section II, LOS parameters are regarded as known information in the attitude estimation of the target. Detailed derivations are as follows.

The ISAR signal is expressed by the superposition of isolated point scatterer responses, and conventional range compression and range cell migration correction are assumed well performed in the following equation [27]:

$$S(\tau, t_m) = \sum \gamma T_p \text{sinc}(\gamma T_p(\tau - \tau_0)) \times \text{rect}\left(\frac{t_m}{T_m}\right) \times \exp\left(-\frac{j4\pi R(t_m)}{\lambda}\right) \quad (2)$$

where  $\text{sinc}(u) = \sin(\pi u)/(\pi u)$  refers to the Sinc function,  $\text{rect}(\bullet)$  represents the rectangle window function,  $\tau$  denotes the fast-time relative to the sampling in the range direction,  $\tau_0$  is the time-delay of a scattering point in current pulse,  $T_p$  and  $T_m$  denote the pulse duration width and the pulse repetition time, respectively,  $\gamma$  represents the chirp rate,  $\lambda$  represents the signal wavelength, and  $R(t_m)$  refers to the uncorrected range residue of the scattering center.

After ideal translation compensation, the distance history of a scattering center is given as the inner product between its position and the instantaneous LOS unit vector in the target Cartesian coordinates as the following equation [34]:

$$R(t_m) = \vec{p} \cdot \vec{k} = z \sin \theta(t_m) + y \cos \theta(t_m) \cos \phi(t_m) + x \cos \theta(t_m) \sin \phi(t_m) \quad (3)$$

where the scattering center position is defined as  $\vec{p} = (x, y, z)^T$ . When the target is under stabilized attitude condition, it is constant during the observation period.

LOS parameters  $\theta(t_m)$  and  $\phi(t_m)$  can be approximated by quadratic functions of the azimuth time, which are given as follows:

$$\theta(t_m) = \theta_0 + \omega_a t_m = \theta_0 + \alpha t_m + \Delta \alpha t_m^2 \quad (4)$$

$$\phi(t_m) = \phi_0 + \omega_\beta t_m = \phi_0 + \beta t_m + \Delta \beta t_m^2 \quad (5)$$

where  $\theta_0$  and  $\phi_0$  are the LOS angles corresponding to a single-frame RD image,  $\omega_a = \alpha + \Delta \alpha t_m$  denotes the velocity of the elevation angle, and  $\omega_\beta = \beta + \Delta \beta t_m$  denotes the velocity of the azimuth angle.

Combined with the approximation formula (6), the distance history (3) is rewritten as (7)

$$\begin{cases} \sin(\theta + \omega t) \approx \sin \theta + \cos \theta \cdot \omega t \\ \cos(\theta + \omega t) \approx \cos \theta - \sin \theta \cdot \omega t \end{cases} \quad (6)$$

$$R(t_m) = R_0(x, y, z) + R_1(x, y, z)t_m + R_2(x, y, z)t_m^2 \quad (7)$$

$$\begin{cases} R_0(x, y, z) = \vec{\mathbf{r}}_0 \cdot \vec{\mathbf{p}} \\ R_1(x, y, z) = \vec{\mathbf{r}}_1 \cdot \vec{\mathbf{p}} \\ R_2(x, y, z) = \vec{\mathbf{r}}_2 \cdot \vec{\mathbf{p}} \end{cases} \quad (11)$$

$$\vec{\mathbf{r}}_0 = \begin{bmatrix} \cos \theta_0 \sin \phi_0 \\ \cos \theta_0 \cos \phi_0 \\ \sin \theta_0 \end{bmatrix}^T$$

$$\vec{\mathbf{r}}_1 = \begin{bmatrix} \cos \theta_0 \cos \phi_0 \cdot \beta - \sin \theta_0 \sin \phi_0 \cdot \alpha \\ -\cos \theta_0 \sin \phi_0 \cdot \beta - \sin \theta_0 \cos \phi_0 \cdot \alpha \\ \cos \theta_0 \cdot \alpha \end{bmatrix}^T$$

$$\vec{\mathbf{r}}_2 = \begin{bmatrix} \cos \theta_0 \cos \phi_0 \cdot \Delta\beta - \sin \theta_0 \sin \phi_0 \cdot \Delta\alpha - \sin \theta_0 \cos \phi_0 \cdot \alpha\beta \\ -\cos \theta_0 \sin \phi_0 \cdot \Delta\beta - \sin \theta_0 \cos \phi_0 \cdot \Delta\alpha + \sin \theta_0 \sin \phi_0 \cdot \alpha\beta \\ \cos \theta_0 \cdot \Delta\alpha \end{bmatrix}^T \quad (12)$$

where the constant term, the first-order term and the quadratic term are given as the following equations:

$$R_0(x, y, z) = z \sin \theta_0 + y \cos \theta_0 \cos \phi_0 + x \cos \theta_0 \sin \phi_0 \quad (8)$$

$$\begin{aligned} R_1(x, y, z) &= z \cos \theta_0 \cdot \alpha \\ &\quad - y[\cos \theta_0 \sin \phi_0 \cdot \beta + \sin \theta_0 \cos \phi_0 \cdot \alpha] \\ &\quad + x[\cos \theta_0 \cos \phi_0 \cdot \beta - \sin \theta_0 \sin \phi_0 \cdot \alpha] \end{aligned} \quad (9)$$

$$\begin{aligned} R_2(x, y, z) &= z \cos \theta_0 \cdot \Delta\alpha \\ &\quad - y[\cos \theta_0 \sin \phi_0 \cdot \Delta\beta + \sin \theta_0 \cos \phi_0 \cdot \Delta\alpha] \\ &\quad + x[\cos \theta_0 \cos \phi_0 \cdot \Delta\beta - \sin \theta_0 \sin \phi_0 \cdot \Delta\alpha] \\ &\quad + y[\sin \theta_0 \sin \phi_0 \cdot \alpha\beta] - x[\sin \theta_0 \cos \phi_0 \cdot \alpha\beta]. \end{aligned} \quad (10)$$

In the case of the conventional RD processing, the radar signal  $S(\tau, t_m)$  is transferred to RD domain with an azimuth fast Fourier transform (FFT) to obtain a focused image  $f(n, m)$ . Thus, the connection between the distance history and the RD imagery is as follows: the constant phase coefficient  $R_0(x, y, z)$  represents the initial distance of the point, the first-order phase coefficient  $R_1(x, y, z)$  determines the azimuth Doppler coordinate, and the residual quadratic phase coefficient  $R_2(x, y, z)$  causes the defocusing phenomenon of the RD image. In practical applications, the residual quadratic phase degrades the image quality and usually is considered as an undesired error factor. Several autofocusing algorithms have been developed for the residual phase adjustment [20]–[23], [28]–[30]. Compared with these references, this paper makes a significant difference in handling the spatial-variant quadratic phase characteristic. It is considered as important as other phase information and is utilized to interpret the target attitude with priori target structural characteristics.

First, the range history is presented in vector as in (11) and (12), shown at the top of this page.

Scattering points distributed in a 2-D plane  $P(x, y, z)$  can be expressed as a set with the inner product expression

$$\vec{\mathbf{V}}_T \cdot P(x, y, z) = \varepsilon \quad (13)$$

where  $\vec{\mathbf{V}}_T$  represents the normal vector of the plane component,  $\varepsilon$  is the distance of the origin from the plane and equals 0 when the coordinate origin is contained in the plane as drawn in Fig. 1(b). It ought to be stated that attitude analysis of the target and that of the key plane component are equivalent in this paper, because the attitude of the key plane component directly reflects the operational state and potential intention of the observed target.

On the other hand, the spatial-variant phase error is proportional to the range and Doppler coordinate of the scattering point in the RD image. It is expressed as a linear function in the relevant literature [28]–[30]

$$R_2(x, y, z) = e_r R_0(x, y, z) + e_a R_1(x, y, z). \quad (14)$$

By substituting (11) into (14), an explicit expression bridging the defocusing performance and the target attitude parameters is obtained

$$e_r \vec{\mathbf{r}}_0 \cdot P(x, y, z) + e_a \vec{\mathbf{r}}_1 \cdot P(x, y, z) - \vec{\mathbf{r}}_2 \cdot P(x, y, z) = \varepsilon. \quad (15)$$

Hence,  $\vec{\mathbf{V}}_T$  can be solved with defocusing coefficients  $e_r$  and  $e_a$

$$\vec{\mathbf{V}}_T = e_r \vec{\mathbf{r}}_0 + e_a \vec{\mathbf{r}}_1 - \vec{\mathbf{r}}_2. \quad (16)$$

#### IV. ACHIEVING QUADRATIC PHASE COEFFICIENTS BY THE CONTRAST MAXIMIZATION

From the signal derivation mentioned above, we are informed that, if the ISAR image defocusing coefficients  $e_r$  and  $e_a$  are solved exactly, the attitude information of a plane component denoted by  $\vec{\mathbf{V}}_T$  can be determined. It is necessary to stress that the attitude parameter calculation in (16) is based on the assumption that a plane component, such as planar wings and antennas, is loaded in the satellite target. In practical applications, image segmentation techniques ought to be performed to segment out the pixels in the plane component, and detailed processing will be illustrated in the experiment section.

In this section, we will answer the question of how to estimate defocusing coefficients  $e_r$  and  $e_a$  from the RD imagery. According to the distance history (7), image focusing performance will improve if the quadratic spatial-variant phase compensation is successfully performed. If and only if the defocusing coefficients are precisely determined, the image focusing performance can be maximum.

In view of the phase adjustment in ISAR processing, the spatial-variant phase compensation can be performed in the azimuth time domain. It means the unfocused RD image  $f(n, m)$  needs to be transformed by an inverse FFT (IFFT) procedure in the azimuth direction before the compensation

$$S(n, k) = \text{IFFT}[f(n, m)]. \quad (17)$$

According to the quadratic phase error model (14), the spatial-variant quadratic phase compensation is split into range and azimuth-independent components. These two components are represented by the range focusing parameter  $a$  and the azimuth focusing parameter  $b$ , respectively,

$$S'(n, k) = S(n, k) \times \exp(-i\alpha n k^2) \quad (18)$$

$$f'(n, m) = \sum_{k=-\frac{K}{2}}^{\frac{K}{2}-1} S'(n, k) \times \exp\left(-ibm k^2 - \frac{i2\pi m k}{M}\right) \quad (19)$$

where  $n = [-(N/2), \dots, (N/2) - 1]$  denotes the range position in the RD image,  $m = [-(M/2), \dots, (M/2) - 1]$  denotes the Doppler position in the RD image, and  $k = [-(K/2), \dots, (K/2) - 1]$  denotes the azimuth time position of the radar echo data, which bounds up with the radar pulse repetition frequency (PRF) and can be calculated as  $k = t_m \times \text{PRF}$ . In particular, since the quadratic azimuth phase compensation (19) is related to the azimuth position, it should be performed synchronously with the azimuth compression. For this reason, the azimuth compression can no longer be performed by an FFT but a discrete Fourier transform in the azimuth direction to avoid new phase error generated by the FFT procedure.

The contrast, calculated as the ratio of the standard deviation of the pixel magnitude to the pixel magnitude mean, is a well-known quantitative metric to evaluate the imagery focusing quality [21], [30]. It is adopted to compare the focusing performances before and after the phase compensation

$$C(f(n, m)) = \frac{\sigma}{\mu} \quad (20)$$

where  $\mu$  represents the average of pixel amplitudes in the image, and  $\sigma^2$  represents the variance of pixel amplitudes in the image

$$\mu = \frac{1}{MN} \sum_{n=-\frac{N}{2}}^{\frac{N}{2}-1} \sum_{m=-\frac{M}{2}}^{\frac{M}{2}-1} |f(n, m)| \quad (21)$$

$$\sigma = \sqrt{\frac{1}{MN} \sum_{n=-\frac{N}{2}}^{\frac{N}{2}-1} \sum_{m=-\frac{M}{2}}^{\frac{M}{2}-1} (|f(n, m)| - \mu)^2}. \quad (22)$$

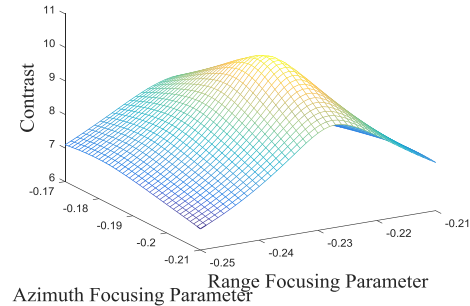


Fig. 4. Contrast function of the quadratic phase coefficients.

Thus, the quadratic phase compensation can be transformed into an unconstrained maximization of the image contrast, and focusing parameters can be obtained by maximizing the contrast function

$$\{\hat{a}, \hat{b}\} = \arg \max_{a, b} C(f(n, m; \{a, b\})). \quad (23)$$

The above-mentioned optimization (23), whose cost function is depicted as Fig. 4, usually does not have multiple local optima. Normally, it can be solved numerically by most quasi-Newton algorithms, such as the Davidon–Fletcher–Powell algorithm and the Broyden–Fletcher–Goldfarb–Shanno (BFGS) algorithm [35], [36]. Actually, it is also an available approach to estimating focusing parameters by adopting 2-D exhaustion or the Monte Carlo method without the limitation of computation time. In this paper, we utilize the BFGS algorithm to solve the optimization (23). The first-order gradient of the RD image contrast corresponding to the compensation parameters are derived as the following equations:

$$\begin{aligned} & \frac{\partial C(f(n, m; \{a, b\}))}{\partial a} \\ &= \frac{1}{\mu} \frac{\partial \sigma}{\partial a} - \frac{\sigma}{\mu^2} \frac{\partial \mu}{\partial a} \\ &= \frac{1}{\mu} \frac{1}{\sigma M N} \sum_{n=-N/2}^{N/2-1} \sum_{m=-M/2}^{M/2-1} (|f(n, m)| - \mu) \frac{\partial |f(n, m)|}{\partial a} \\ &\quad - \frac{\sigma}{\mu^2} \frac{1}{M N} \sum_{n=-N/2}^{N/2-1} \sum_{m=-M/2}^{M/2-1} \frac{\partial |f(n, m)|}{\partial a} \\ &= \frac{1}{\sigma \mu^2 M N} \sum_{n=-N/2}^{N/2-1} \sum_{m=-M/2}^{M/2-1} (\mu |f(n, m)| - \mu^2 - \sigma^2) \frac{\partial |f(n, m)|}{\partial a} \end{aligned} \quad (24)$$

$$\begin{aligned} & \frac{\partial |f(n, m)|}{\partial a} \\ &= \frac{\partial (f(n, m) f^*(n, m))^{\frac{1}{2}}}{\partial a} \\ &= \frac{1}{|f(n, m)|} \text{Re} \left( f(n, m) \frac{\partial f^*(n, m)}{\partial a} \right) \\ &= \text{Re} \left( \frac{f(n, m)}{|f(n, m)|} i n \sum_{k=-M/2}^{M/2-1} k^2 S^*(n, k) \right. \\ &\quad \left. \times \exp(i2\pi km/M + i(an + bm)k^2) \right) \end{aligned} \quad (25)$$

$$\begin{aligned}
& \frac{\partial C(f(n, m; \{a, b\}))}{\partial b} \\
&= \frac{1}{\mu} \frac{\partial \sigma}{\partial b} - \frac{\sigma}{\mu^2} \frac{\partial \mu}{\partial b} \\
&= \frac{1}{\mu} \frac{1}{\sigma M N} \sum_{n=-N/2}^{N/2-1} \sum_{m=-M/2}^{M/2-1} (|f(n, m)| - \mu) \frac{\partial |f(n, m)|}{\partial b} \\
&\quad - \frac{\sigma}{\mu^2} \frac{1}{MN} \sum_{n=-N/2}^{N/2-1} \sum_{m=-M/2}^{M/2-1} \frac{\partial |f(n, m)|}{\partial b} \\
&= \frac{1}{\sigma \mu^2 MN} \sum_{n=-N/2}^{N/2-1} \sum_{m=-M/2}^{M/2-1} (\mu |f(n, m)| - \mu^2 - \sigma^2) \frac{\partial |f(n, m)|}{\partial b}
\end{aligned} \tag{26}$$

$$\begin{aligned}
& \frac{\partial |f(n, m)|}{\partial b} \\
&= \frac{\partial (f(n, m) f^*(n, m))^{\frac{1}{2}}}{\partial b} \\
&= \frac{1}{|f(n, m)|} \operatorname{Re} \left( f(n, m) \frac{\partial f^*(n, m)}{\partial b} \right) \\
&= \operatorname{Re} \left( \frac{f(n, m)}{|f(n, m)|} i m \sum_{k=-M/2}^{M/2-1} k^2 S^*(n, k) \right. \\
&\quad \left. \times \exp(i 2\pi km/M + i(an + bm)k^2) \right). \tag{27}
\end{aligned}$$

The flowchart of the BFGS algorithm is given in Fig. 5, and its key steps are given as follows.

*Step 1 Parameters Initialization:* Set iteration number  $j = 1$ , focusing parameters vector  $\vec{x}_0 = (a_0, b_0)^T = (0, 0)^T$ , gradient threshold  $\varepsilon$ , and initial Hessian matrix  $\mathbf{B}_0 = \mathbf{E}$ . Input unfocused image  $f_0(n, m)$ .

*Step 2 Gradient Calculation of the Image Contrast Evaluating Function:* Combine (24)–(27) to calculate the current gradient of the contrast evaluating function in the following equation:

$$\vec{g}_j = \left( \frac{\partial C(f_{j-1}(n, m; \vec{x}_{j-1}))}{\partial a_{j-1}}, \frac{\partial C(f_{j-1}(n, m; \vec{x}_{j-1}))}{\partial b_{j-1}} \right)^T. \tag{28}$$

*Step 3 Searching Orientation Determination:* Determine the searching orientation with the following equation:

$$\vec{d}_j = \mathbf{B}_{j-1}^{-1} \vec{g}_j. \tag{29}$$

*Step 4 Searching Step Determination:* Based on solving a maximization (30) with a 1-D inexact searching method, the step of searching is determined

$$\lambda_j = \arg \max_{\lambda \in R} C(f_{j-1}(n, m; \vec{x}_{j-1} + \lambda \vec{d}_j)). \tag{30}$$

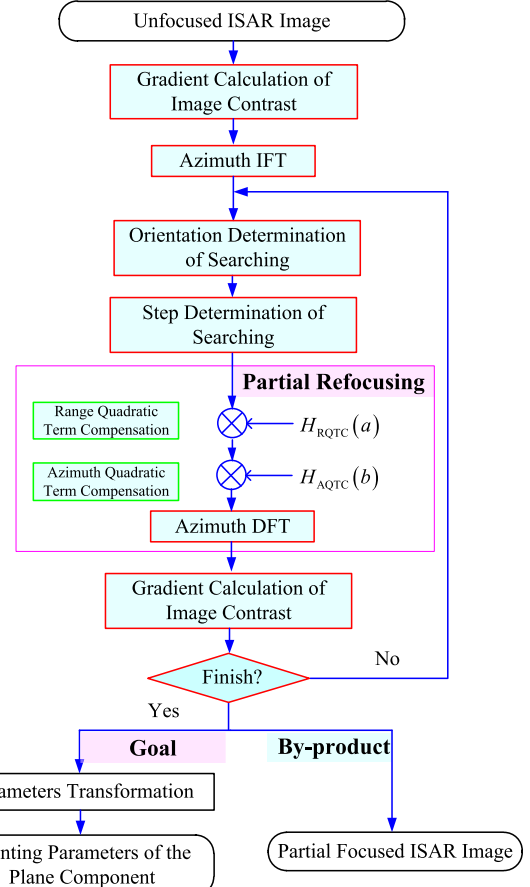


Fig. 5. Flowchart of the BFGS algorithm.

In practical applications, the current acceptable step  $\lambda_j$  is obtained with the Armijo–Goldstein principle as the following equations:

$$\begin{aligned}
C(f_{j-1}(n, m; \vec{x}_{j-1} + \lambda_j \vec{d}_j)) &\geq C(f_{j-1}(n, m; \vec{x}_{j-1})) + \rho \lambda_j \vec{d}_j^T \mathbf{B}_{j-1} \vec{d}_j
\end{aligned} \tag{31}$$

$$\begin{aligned}
C(f_{j-1}(n, m; \vec{x}_{j-1} + \lambda_j \vec{d}_j)) &\leq C(f_{j-1}(n, m; \vec{x}_{j-1})) + (1 - \rho) \lambda_j \vec{d}_j^T \mathbf{B}_{j-1} \vec{d}_j
\end{aligned} \tag{32}$$

where the balance factor  $\rho \in [0.2, 0.4]$ .

*Step 5 Image Focusing:* Set  $\vec{s}_j = \lambda_j \vec{d}_j$ ,  $\vec{x}_j = \vec{x}_{j-1} + \vec{s}_j$ , and substitute them into phase compensation (18), (19) to obtain the partial refocused image  $f_j(n, m)$ . Then, the new gradient calculation of the image contrast evaluating function  $\vec{g}_{j+1}$  can be calculated according to (28).

*Step 6 Iteration Termination Judgment:* If  $\|\vec{g}_{j+1}\| < \varepsilon$ , the iterative searching breaks and the optimal focusing parameter vector  $(\hat{a}, \hat{b})^T = \sum_{q=1}^j \vec{x}_q$  is obtained. Otherwise, correct the Hessian Matrix according to (33) and (34), add iterative number  $j = j + 1$  and return to Step 3

$$\vec{y}_j = \vec{g}_{j+1} - \vec{g}_j \tag{33}$$

$$\mathbf{B}_j = \mathbf{B}_{j-1} + \frac{\vec{y}_j \vec{y}_j^T}{\vec{y}_j^T \vec{s}_j} - \frac{\mathbf{B}_{j-1} \vec{s}_j \vec{s}_j^T \mathbf{B}_{j-1}}{\vec{s}_j^T \mathbf{B}_{j-1} \vec{s}_j}. \tag{34}$$

TABLE I  
MAIN PARAMETERS OF ISAR SYSTEM

Size of Images	$256 \times 512$
Wave Length of the Signal	0.018 m
Bandwidth	750 MHz
Sample Frequency	1.5 GHz
Center Frequency of Transmit Signal	16.7 GHz
Pulse Repetition Frequency	50 Hz

When the optimal focusing parameters  $\hat{a}$  and  $\hat{b}$  are solved, the original image defocusing coefficients  $e_r$  and  $e_a$  can be calculated as follows:

$$e_r = -\frac{\lambda pr f^2}{4\pi \Delta r} \hat{a} \quad (35)$$

$$e_a = \frac{\lambda pr f^2}{4\pi \Delta f_d} \hat{b} \quad (36)$$

where  $\Delta r = c/2f_s$  denotes the range

## V. EXPERIMENT ANALYSIS

In this section, the capability of the proposed algorithm will be assessed by three simulation experiments.

- 1) First of all, a rectangular scattering point array is used as the observed target to investigate the capability of the proposed algorithm. The observation station is set at Beijing (39.9 N, 116.4 E, 0 m) and the target TLE parameters are adopted with an LEO satellite at an altitude of 400 km.
- 2) In order to demonstrate the effectiveness of the proposed algorithm in practical tasks, a typical satellite target, the Aura satellite, replaces the plane scattering point array as the observed target for attitude estimation in two different attitudes. We also validate the steadiness of the proposed algorithm by an antinoise jamming experiment in this part.
- 3) As an extension part, a multistatic algorithm is explored to improve the robustness of the proposed algorithm in practical scenarios. In this experiment, Tianjin (39.1 N, 117.2 E, 0 m) station is added into the observation system with Beijing station. We also illustrate the meaningful progress of the proposed algorithm in the radar resource utilization through a comparison with a previous work.

For lack of access to real measured ISAR data, the proposed algorithm is investigated with ISAR simulation images. All simulation uses a Ku-band ISAR system, whose main system parameters are given in Table I, and the 3-D model of the Aura satellite is shown in Fig. 6. The pointlike high-frequency simulation strategy is adopted in the signal generation of Part A, while the improved physical optical algorithm with facet model is applied to generate radar echo data in Parts B and C, according to [31]. By the RD imaging algorithm, the acquired RD images are approximately the practical measured ISAR ones, which supports the investigation for practical applications [31], [32].

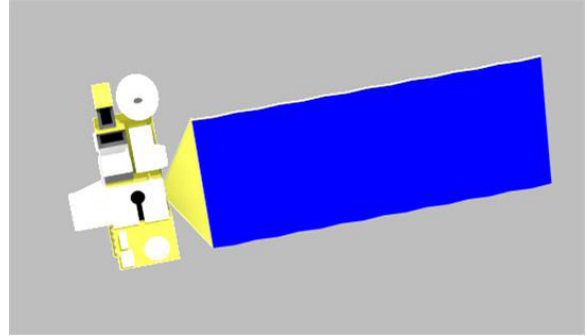


Fig. 6. 3-D model of the Aura satellite.

### A. Demonstration Experiments With a Planar Scattering Point Array

In this section, the capability of the proposed algorithm is demonstrated by the attitude determination for a plane component in a satellite, which is composed of a rectangle scattering point array. Generally, it should be avoided to perform the proposed algorithm in the zenith-passing duration of the satellite target observation, when the elevation angle  $\theta$  nears to the maximum in the current trajectory. As the LOS parameters rapidly change during this period, high-order phase terms would be present in the signal, besides the useful quadratic terms in (4) and (5). Consequently, the quadratic phase coefficient estimation degrades dramatically. As shown in Fig. 7, the proposed algorithm is tested individually at Times 1, 2, and 3. The coherent processing interval of each RD image is around  $3^\circ$  to guarantee that the azimuth resolution (actually is replaced with the Doppler resolution after RD imaging in this paper) is of the same magnitude as the range resolution. As mentioned earlier, due to the varying LOS relative to the target, a three-axis stabilized target is projected with different poses in these three images. Moreover, as shown in the first column of Fig. 8, an apparent regularity in these three images is concluded as the defocusing level of each scattering point performs differently and it almost displays a symmetrical distribution around the scene center. This phenomenon coincides exactly with the quadratic phase error presentation in (14). Later, target attitudes are estimated via the BFGS algorithm, and focused images can be obtained as a by-product.

The second column of Fig. 8 presents quadratic phase compensation results, where the improvement of image contrast is apparent compared with the original images in the first column. In addition, Table II lists the attitude estimation results, together with the numerical changes of image contrast. In order to illustrate our work visually, a visual comparison between estimation attitude (marked green) and true attitude (marked red) is presented in the third column of Fig. 8. The results illustrate the feasibility of the proposed algorithm.

### B. Demonstration Experiments With a Typical Satellite

Following the previous experiment, two examples are investigated for the attitude estimation of a typical satellite by utilizing the proposed algorithm in this part. Different from

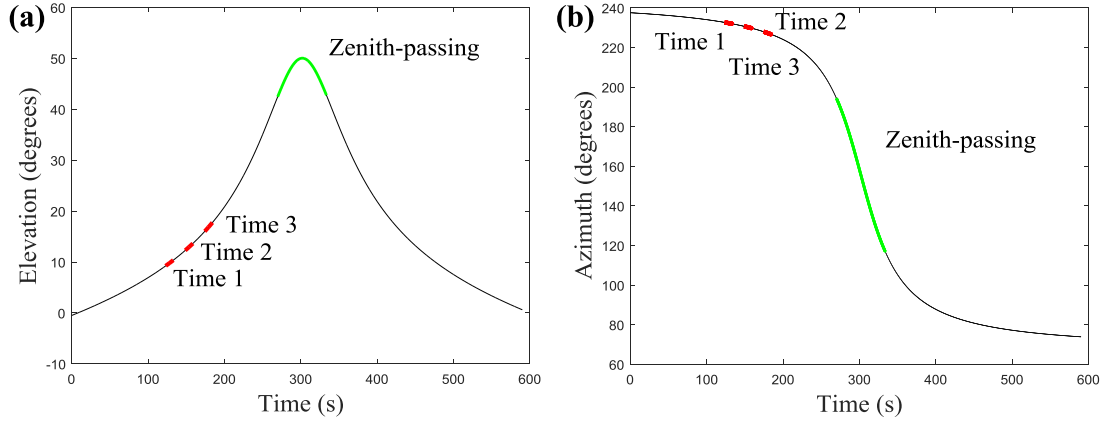


Fig. 7. LOS parameters selection of the observation. (a) Elevation angle curve. (b) Azimuth angle curve.

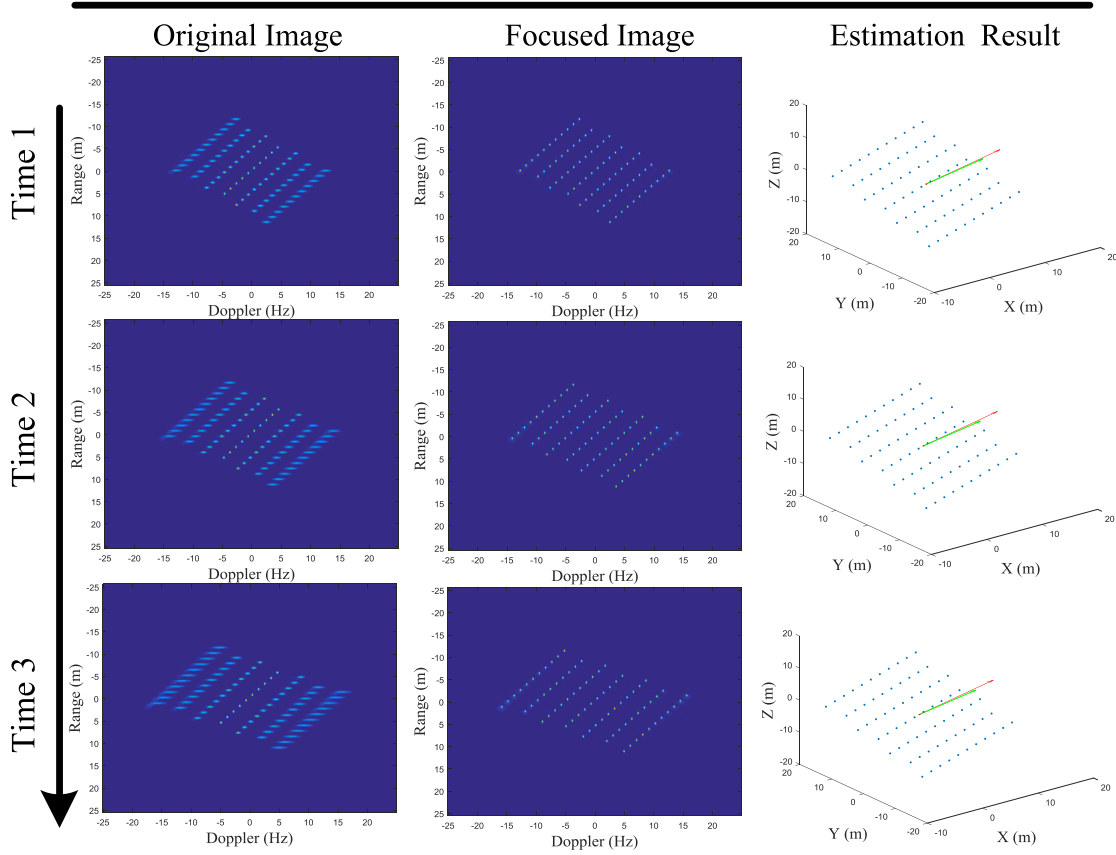


Fig. 8. Estimation processing of the plane array.

TABLE II  
ESTIMATION RESULTS OF THE PLANE ARRAY

Image Number	Defocusing Parameter $e_r (\times 10^{-4})$	Defocusing Parameter $e_a$	Image Contrast Before Refocus	Image Contrast After Refocus	Estimation Attitude	Error
Frame 1	-2.004	0.0182	6.7432	10.2849	(0.9460, 0.3241, -0.0088)	1.20 degrees
Frame 2	-2.458	0.0219	6.2315	10.3107	(0.9468, 0.3213, -0.0191)	1.66 degrees
Frame 3	-3.092	0.0265	5.4469	9.5747	(0.9440, 0.3285, -0.0297)	1.89 degrees

In the previous experiment, the same LOS parameters are chosen to generate a continuous RD image sequence composed of three frames to estimate the target attitude at Time 1.

During the contiguous imaging period, the sliding window strategy is adopted to process the echo data, and the total radar observation angular scope of these three images adds up

TABLE III  
ESTIMATION RESULTS OF THE AURA SATELLITE

Image Number	Image Contrast Before Refocus	Image Contrast After Refocus	True Attitude	Estimation Attitude	Error
<b>Pose I</b>					
Frame 1	3.1410	3.4922	(0.9397, 0.3420, 0.0000)	(0.9457, 0.3243, -0.0243)	1.75 degrees
Frame 2	3.1008	3.4634	(0.9397, 0.3420, 0.0000)	(0.9454, 0.3256, -0.0134)	1.23 degrees
Frame 3	3.0557	3.4174	(0.9397, 0.3420, 0.0000)	(0.9458, 0.3236, -0.0289)	2.00 degrees
After Weighting				(0.9456, 0.3245, -0.0222)	1.70 degrees
<b>Pose II</b>					
Frame 1	3.4728	3.7969	(0.8660, 0.5000, 0.0000)	(0.8904, 0.4552, -0.0023)	2.92 degrees
Frame 2	3.4223	3.7730	(0.8660, 0.5000, 0.0000)	(0.8943, 0.4473, -0.0135)	3.51 degrees
Frame 3	3.3610	3.7202	(0.8660, 0.5000, 0.0000)	(0.8970, 0.4407, -0.0349)	4.32 degrees
After Weighting				(0.8930, 0.4477, -0.0169)	3.63 degrees

to  $4.71^\circ$ . Aiming at reducing the error from the echo quality disturbance, the attitude estimation result of the whole image sequence is obtained by weighting the estimation result of each frame. Considering that the target will be projected to different RD imaging planes in different poses, we conclude that the contrast value cannot directly indicate the focusing performance among different RD image frames. Thus, a principle is presented to average the estimation results of multiple image frames

$$\hat{V}_T = \frac{1}{N} \sum_{i=1}^N \frac{(e_{ri}, e_{ai}, -1)^T}{|(e_{ri}, e_{ai}, -1)^T|} \quad (37)$$

where  $i$  refers to the index number of a certain RD image frame.

Another apparent distinction from the former is the input image of the estimation task. An image segmentation is embedded in the attitude estimation to capture the plane part (i.e., the solar wing) in the satellite target, which represents the target attitude information effectively.

*Image Segmentation Process:* In order to ensure the quality of the estimation, the segmentation aims at cutting out a considerable area of the plane component, where fewer other scattering points exist in the same range cell. Usually, the plane component is confined with a quadrilateral, and the inside point is located between two sets of opposite side. Based on this, a simple judgment of shape segmentation is explicitly expressed as

$$L_1(n, m) \cdot L_2(n, m) < 0 \quad (38)$$

$$L_3(n, m) \cdot L_4(n, m) < 0 \quad (39)$$

where  $L_i(n, m)$  is the functional expression of the quadrilateral sides, which can be determined with four vertexes, index number  $i = 1, 2, 3, 4$ .  $L_1(n, m)$  and  $L_2(n, m)$  compose a pair of opposite side, and  $L_3(n, m)$  and  $L_4(n, m)$  compose the other.

For the first example, a three-axis stabilized satellite with the specific attitude I is measured. Fig. 9(a) shows the original integral image while the partial solar wing image is acquired

by the segmentation, as shown in Fig. 9(b). Through the proposed algorithm, this partial image is refocused as given in Fig. 9(d), and the focusing parameters are also used to refocus the integral image. It can be obviously observed that the solar wing part shows better-focusing performance after the refocusing [i.e., the circled part in Fig. 9(d)]. Compared with the original integral image, the focusing performance of the refocused integral image is also improved, as shown in the circled part in Fig. 9(c). Although focusing quantity evaluating indicators can hardly be given such as peak sidelobe ratio, integrated sidelobe ratio, and impulse response width, due to the target size characteristic of ISAR images, the visual comparison of the azimuth profiles of the same range cell [depicted as green lines in Fig. 9(a) and (c)] before and after the refocusing in Fig. 9(e) illustrates the improvement of the focusing performance. Finally, the contrast change and estimation results are listed in Table III. In order to assess the performance comparison of the estimated attitude (marked green) and the true attitude (marked red), we also make a visual comparison in Fig. 9(f). The visual comparison result adequately demonstrates the feasibility of the proposed algorithm.

In the second example, with the target attitude changed, a repeated experiment is designed to illustrate the applicability of the proposed algorithm in different LOS parameters. Similarly, the image refocusing and attitude estimation results are provided in Fig. 10 and Table III. It should be emphasized that the contrast of the integral image can hardly achieve the optimum in this approach since ideal focusing parameters vary from one plane to another in the same RD image. Regarding the refocused imagery as a by-product, we do not take multiple planes segmentation of the target surface into consideration to get a fine focused integral image in this paper.

Previous experiments validate the feasibility and accuracy of the proposed algorithm. Furthermore, in order to investigate the sensitivity of the proposed algorithm against random noise, attitude estimation experiment is repeated under additive white Gaussian noise conditions. The signal-to-noise ratio (SNR) of

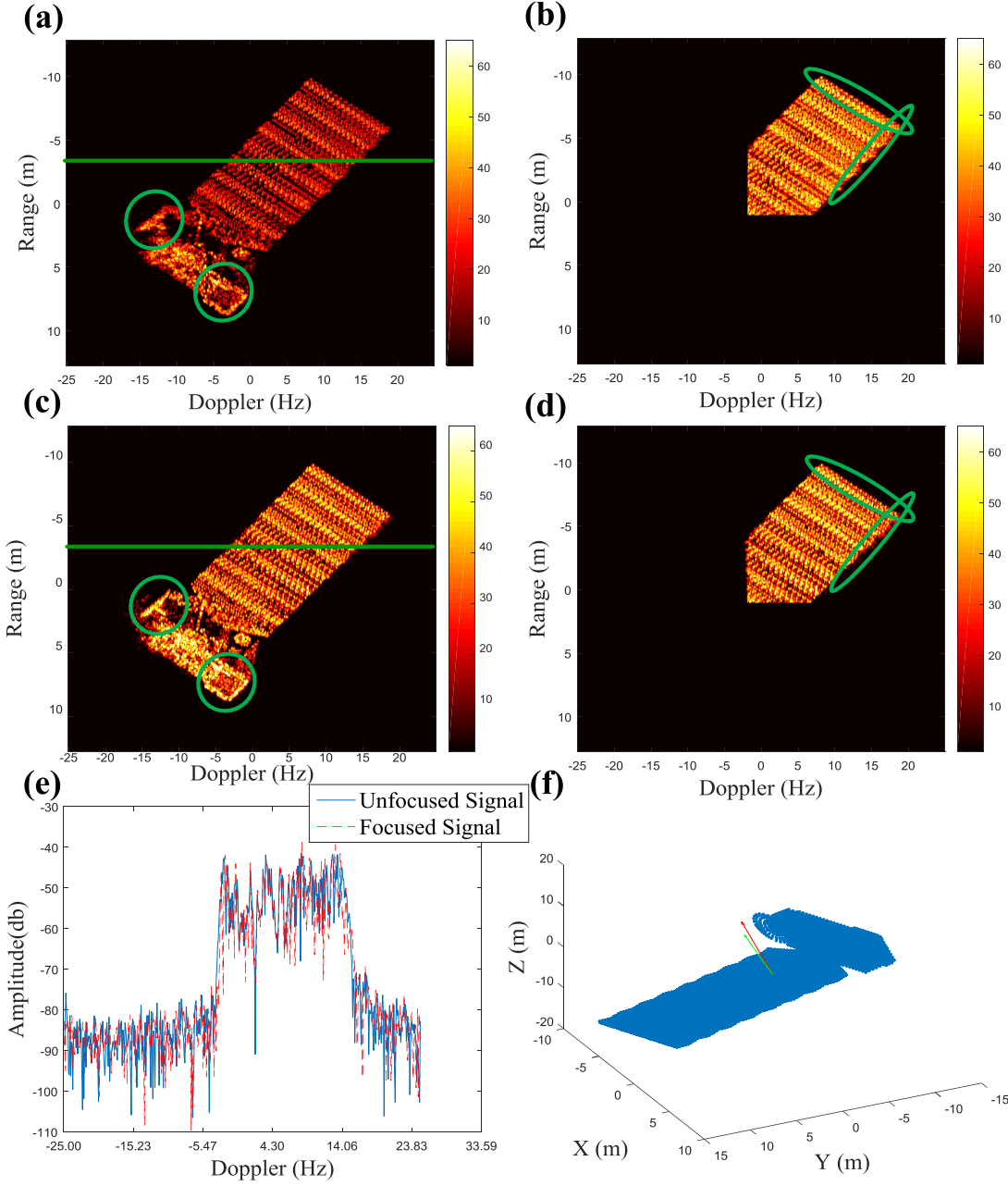


Fig. 9. Estimation results of Aura satellite in pose I. (a) Original RD image. (b) Partial solar wing image. (c) Integral image after refocusing. (d) Segmented integral image after refocusing. (e) Comparison of the azimuth pulse responses of a certain range cell. (f) Visual comparison between estimated attitude and true attitude.

a signal is defined as

$$\text{SNR} = 10\log_{10}(E_s/E_n) \quad (40)$$

where  $E_s$  denotes the energy of the radar echo after range pulse compression, and  $E_n$  denotes the energy of the additive white Gaussian noise.

The estimation error curve in Fig. 11 reveals the performance of the proposed algorithm in different noise conditions. It is evident that though radar echo data are contaminated by noise, the proposed algorithm still obtains attitude estimation results with high precision, even when the SNR is 0 dB. It validates the robustness of the proposed algorithm against noise and jamming.

#### C. Extension Experiments With the Multistatic Observation

As an extension of the proposed algorithm, a multistatic algorithm is investigated to improve its capability of multistatic collaboration in practical applications. The multistatic method is also built on aforementioned stabilized attitude assumption of the target. According to this assumption, the observed target will keep a steady attitude in the target Cartesian coordinates during the multistatic observation. Under this observation model, various target poses are projected in different RD imaging planes with diverse observation views. It increases the redundancy of the observation data, which helps to overcome the observation view sensibility of the single-station algorithm to attain a more robust estimation result.

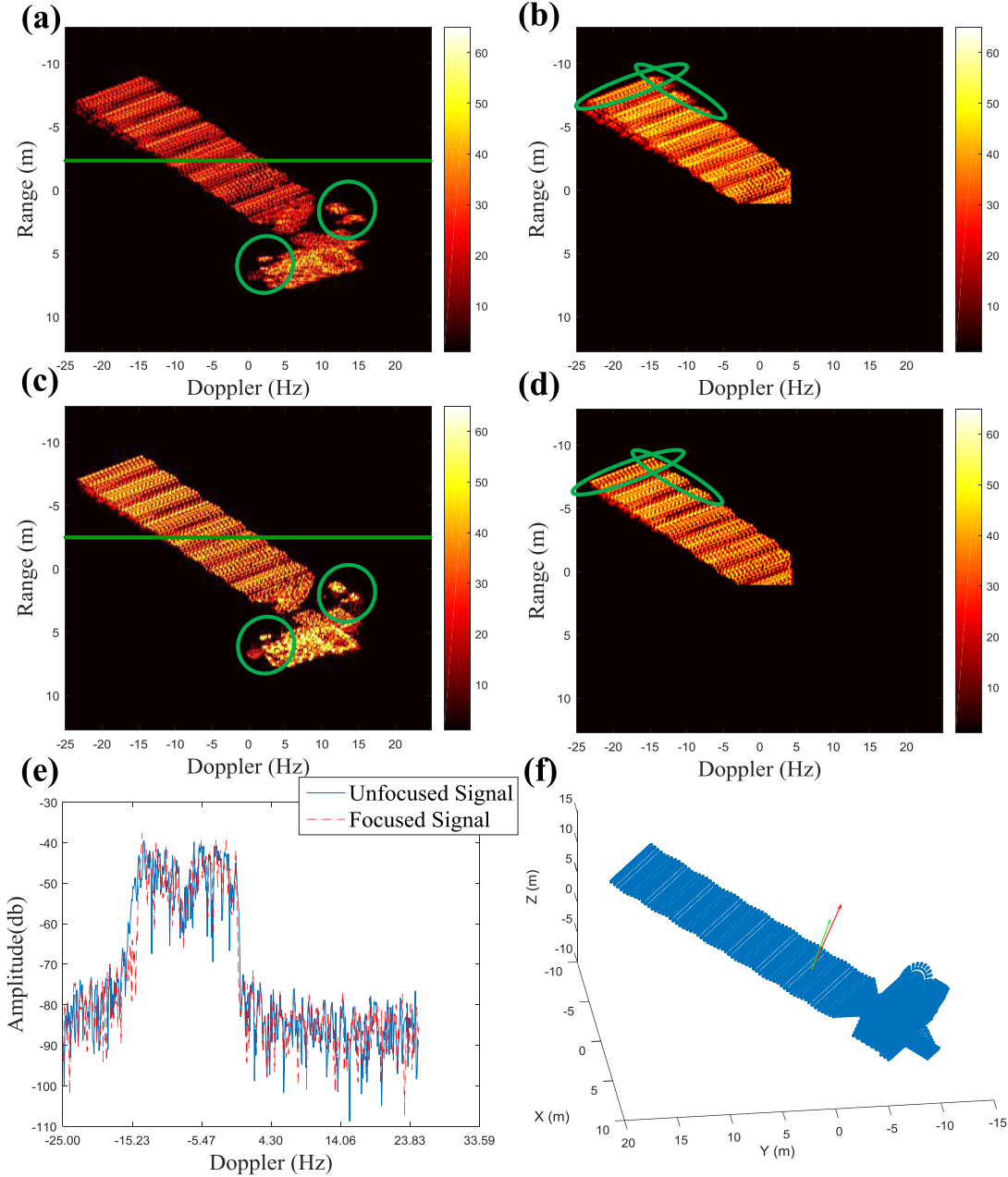


Fig. 10. Estimation results of Aura satellite in pose II. (a) Original RD image. (b) Partial solar wing image. (c) Integral image after refocusing. (d) Segmented integral image after refocusing. (e) Comparison of the azimuth pulse responses of a certain range cell. (f) Visual comparison between estimated attitude and true attitude.

For example, as shown in Fig. 12, we take Beijing station and Tianjin station as a bistatic observation system to validate the functionality of the multistatic algorithm. During the observation of each radar station, three sequential images are generated to solve three attitude vectors of the solar wing parts independently. Following the joint estimation principle (37), these three attitude vectors are weighted to represent the instantaneous attitude of the solar wing at Time 2. The SNR of each RD image is set at 10 dB, and the observation angular scopes of Beijing station and Tianjin station are  $5.90^\circ$  and  $5.69^\circ$ , respectively. The detailed processing is shown in Fig. 13, and the attitude results are listed in Table IV. It is evident that compared with the estimation result of single

imagery, the estimation accuracy of the weighted result can be ensured with the redundant observation. With the target attitude solved, we also utilize the target 3-D model to reconstruct these two observation sequences by the generation method of the simulation image [31]. The reconstruction results are given in the fifth column of Fig. 13. As we can see, there is almost no distinction of the projected target pose between the original sequence and the reconstruction in most cases, while it displays a little bias in the last image of Beijing station observation due to the  $2.55^\circ$  estimation bias error.

In order to expound the advantage of the short observation duration requirement, we compare the proposed algorithm with our previous work. In our previous work, the 3-D attitude

TABLE IV  
ESTIMATION RESULTS OF THE BISTATIC OBSERVATION

Image Number	Image Contrast Before Refocus	Image Contrast After Refocus	Estimation Attitude	Error
Tianjin Station				
Frame 1	3.5972	3.7516	(0.9498, 0.3080, -0.0548)	3.74 degrees
Frame 2	3.3796	3.6235	(0.9556, 0.2778, -0.0986)	6.80 degrees
Frame 3	3.1431	3.4220	(0.9404, 0.3343, -0.0630)	3.63 degrees
Beijing Station				
Frame 1	3.2614	3.4861	(0.9624, 0.2715, -0.0015)	4.25 degrees
Frame 2	3.1079	3.3766	(0.9534, 0.3004, -0.0286)	2.99 degrees
Frame 3	2.8315	3.2138	(0.9485, 0.3151, -0.0332)	2.50 degrees
After Weighting			(0.9452, 0.3240, -0.0404)	2.55 degrees

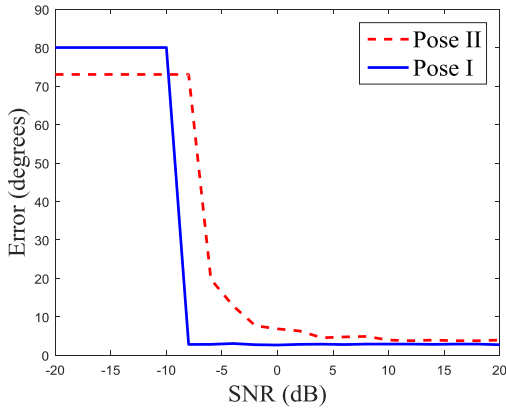


Fig. 11. Curve of estimation error change in different SNR conditions.



Fig. 12. Bistatic observation diagram in STK.

estimation for satellite targets is based on the typical structural feature inversion from an ISAR image sequence [33]. With the ISAR imaging projection, geometry determined [34], the projection orientations of typical structures in RD images are utilized to solve the attitude parameters in a minimization. In order to ensure the stability of the optimization, a considerable long-time observation is required for the redundancy of the observation data. We adopt the same ISAR observation

resource in this paper to reproduce our previous work, and the estimation error curves of the observation duration are shown in Fig. 14. From the error curves in Fig. 14(a), it can be concluded that under the single-station mode, it is difficult to obtain an ideal estimation result by the previous method with a littish angular observation. Even in a bistatic observation, it also needs around 100-s observation to ensure a  $4^\circ$  estimation bias as shown in Fig. 14(b). In this case, the observation angular scopes of Beijing station and Tianjin station add up to  $9.46^\circ$  and  $9.13^\circ$ , respectively. When the feature extraction bias error is taken into consideration, it usually requires a largish angular scope observation over  $15^\circ$  in practical applications.

By contrast, the proposed algorithm requires an around  $6^\circ$  observation to control the estimation error in the same degree. Actually, it merely needs a single image to obtain a single estimation in most cases. Therefore, it is evident that the proposed algorithm makes significant progress in efficient utilization of angular observation resource. Moreover, littish angular observation demand also reduces the objective stability requirement of the target attitude. It inspires us to explore the potential possibility of the attitude estimation for a faulty satellite target, whose attitude changes during a long-time observation.

#### D. Performance Investigation

Generally, the proposed algorithm effectively combines prior structural characteristic and ISAR imaging geometry information to obtain accurate target attitude information. Through the above-mentioned analysis, estimation results illustrate the effectiveness of the proposed algorithm and the extension experiment investigates its practical value for the collaboration observation. In the experiment investigation, we also find some limitations of the proposed algorithm which affect the performance of target attitude estimation. Although some remedial measures have been adopted in this paper, we still ought to pay attention to these limitations in practical applications.

First, in some special combinations of observation visual angle and target attitude, the plane component will be projected as a thin parallelogram or even a line in RD image,



Fig. 13. Estimation processing of the bistatic observation.

which causes the norm of the planar characteristic to decrease. As a result, the connection between the image defocusing performance and the target attitude parameters no longer corresponds to (15), and the attitude estimation might lead to a wrong solution. This potential geometric trouble motivates the multistatic design in this paper. We hope redundant observation will provide enough RD images to avoid the weakness of the planar characteristic in a single-station observation. Coupled with multistation collaboration, the proposed algorithm has really simple demand of time synchronization and consistency of the radar system parameters, but radar net collaboration is still a significant challenge nowadays.

The second is image segmentation. Theoretically speaking, the attitudes of several partial planes can be estimated

after the multiple planes segmentation of the target surface. However, the multiple planes segmentation in the satellite target imagery is difficult to realize nowadays. Thus, the attitude of the major plane component is estimated by the proposed algorithm at the present stage. In the case of the Aura satellite, the solar wing is to be segmented out from the integral image. Even for this single plane, the precision of attitude estimation varies with different segmentation results, because the echo signal of other scattering points in the same range cell impacts the defocusing coefficients estimation of the plane component after the image segmentation. This influence always exists, and one measure is to increase the segmented area of the planar component as mentioned earlier. In addition, from the experiment results, it is believed that the short-duration sequence joint strategy is necessary in order to control the

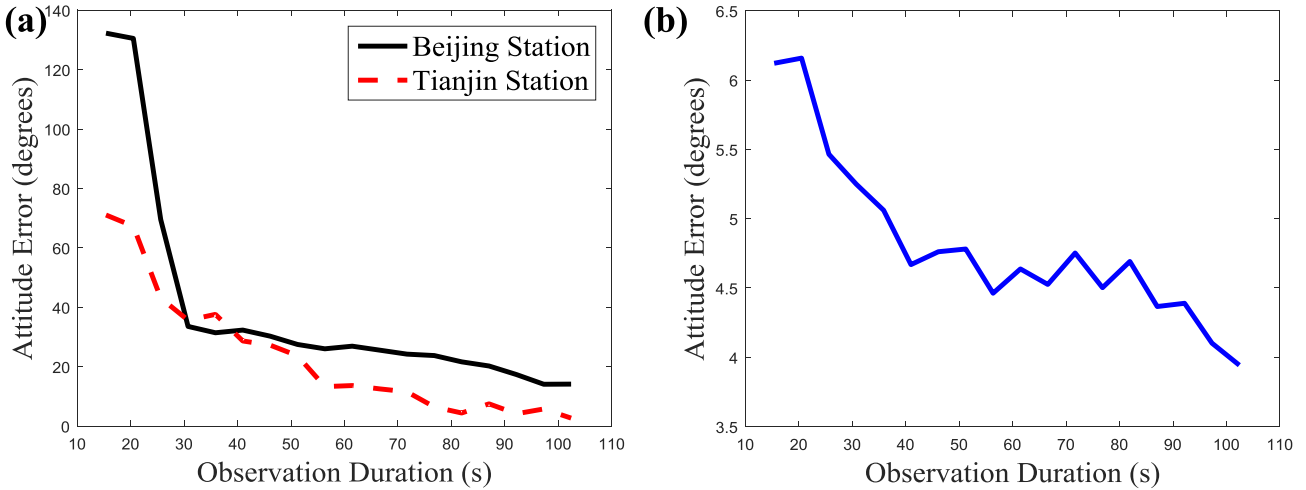


Fig. 14. Estimation error curves of the observation duration. (a) Estimation error curve of the previous single-station method. (b) Estimation error curve of the previous bistatic station method.

estimation bias, especially when some partial shelter or loss of the plane component occurs.

## VI. CONCLUSION

In this paper, in order to estimate the attitude of satellite targets, a motion and geometric projection of ISAR imaging are developed. An explicit expression is derived to connect the image defocusing phenomenon and the attitude information of the satellite target. With prior LOS parameters, the estimation of the satellite target is solved with a maximization of the RD image contrast via the spatial-variant quadratic phase error compensation. The experiment results confirm the effectiveness of the proposed algorithm and a multistatic algorithm is presented as an extension. In practical applications, the estimated normal vectors of plane component can be applied to analyze the target absolute attitude. The work is also potential of integrating with line components on the target [33]. Compared with the previous work, the proposed algorithm has an advantage in the radar resource utilization. Therefore, we believe this paper provides an effective approach to accomplishing the attitude estimation of satellite targets, and it also inspires us to explore the potential possibility of the attitude estimation for faulty satellite targets.

## ACKNOWLEDGMENT

The authors would like to thank the anonymous reviewers for their valuable comments to improve this paper quality.

## REFERENCES

- [1] N. Bobrinsky and L. Del Monte, "The space situational awareness program of the European space agency," *Cosmic Res.*, vol. 48, no. 5, pp. 392–398, 2010.
- [2] *Haystack Ultrawideband Satellite Imaging Radar*, MIT Lincoln Lab., Lexington, MA, USA, Sep. 2014.
- [3] F. Wang, F. Xu, and Y.-Q. Jin, "Three-dimensional reconstruction from a multiview sequence of sparse ISAR imaging of a space target," *IEEE Trans. Geosci. Remote Sens.*, vol. 56, no. 2, pp. 611–620, Feb. 2018.
- [4] J. Šilhá, J.-N. Pittet, M. Hamara, and T. Schildknecht, "Apparent rotation properties of space debris extracted from photometric measurements," *Adv. Space Res.*, vol. 61, no. 3, pp. 844–861, 2017.
- [5] F. Santi, D. Pastina, and M. Bucciarelli, "Estimation of ship dynamics with a multiplatform radar imaging system," *IEEE Trans. Aerosp. Electron. Syst.*, vol. 53, no. 6, pp. 2769–2788, Dec. 2017.
- [6] X. L. Yang, G. J. Wen, J. R. Zhong, B. W. Hui, and C. H. Ma, "A 3-D electromagnetic-model-based algorithm for absolute attitude measurement using wideband radar," *IEEE Geosci. Remote Sens. Lett.*, vol. 12, no. 9, pp. 1878–1882, Sep. 2015.
- [7] S. D'Amico, M. Benn, and J. L. Jørgensen, "Pose estimation of an uncooperative spacecraft from actual space imagery," in *Proc. 5th Int. Conf. Spacecraft Formation Flying Missions Technol.*, 2013, pp. 1–8.
- [8] R. Perrier, E. Arnaud, P. Sturm, and M. Ortner, "Satellite image registration for attitude estimation with a constrained polynomial model," in *Proc. IEEE Int. Conf. Image Process.*, Sep. 2010, pp. 925–928.
- [9] R. Kanzler *et al.*, "Space debris attitude simulation—IOTA (in-orbit tumbling analysis)," in *Proc. Adv. Maui Opt. Space Survill. Technol.*, 2015, pp. 1–13.
- [10] K. Suwa, T. Wakayama, and M. Iwamoto, "Three-dimensional target geometry and target motion estimation method using multistatic ISAR movies and its performance," *IEEE Trans. Geosci. Remote Sens.*, vol. 49, no. 6, pp. 2361–2373, Jun. 2011.
- [11] W.-J. Zhong, J.-S. Wang, W.-J. Ji, X. Lei, and X.-W. Zhou, "The attitude estimation of three-axis stabilized satellites using hybrid particle swarm optimization combined with radar cross section precise prediction," *Proc. Inst. Mech. Eng. G, J. Aerosp. Eng.*, vol. 230, no. 4, pp. 713–725, 2016.
- [12] S. Lemmens, H. Krag, J. Rosebrock, and I. Carnelli, "Radar mappings for attitude analysis of objects in orbit," in *Proc. 6th Eur. Conf. Space Debris*, Darmstadt, Germany, 2013, pp. 20–24.
- [13] J. Rosebrock, "Absolute attitude from monostatic radar measurements of rotating objects," *IEEE Trans. Geosci. Remote Sens.*, vol. 49, no. 10, pp. 3737–3744, Oct. 2011.
- [14] C. Tomasi and T. Kanade, "Shape and motion from image streams under orthography: A factorization method," *Int. J. Comput. Vis.*, vol. 9, no. 2, pp. 137–154, Nov. 1992.
- [15] M. Ferrara, G. Arnold, and M. Stuff, "Shape and motion reconstruction from 3D-to-1D orthographically projected data via object-image relations," *IEEE Trans. Pattern Anal. Mach. Intell.*, vol. 31, no. 10, pp. 1906–1912, Oct. 2009.
- [16] E. McFadden, B. Zhang, and M. Xing, "Three-dimensional reconstruction from ISAR sequences," *Proc. SPIE*, vol. 4744, no. 1, pp. 58–68, Jul. 2002, doi: [10.1117/12.488289](https://doi.org/10.1117/12.488289).
- [17] G. Li, J. Zou, S. Xu, B. Tian, and Z. Chen, "A method of 3D reconstruction via ISAR sequences based on scattering centers association for space rigid object," *Proc. SPIE*, vol. 9252, no. 1, p. 92520N, Oct. 2014, doi: [10.1117/12.2067006](https://doi.org/10.1117/12.2067006).
- [18] *Navstar GPS Space Segment/Navigation User Interfaces*, document ICD-GPS-200C, ARINC Research Corporation, El Segundo, CA, USA, Jan. 2003. [Online]. Available: <https://www.navcen.uscg.gov/pubs/gps/icd200/default.html>

- [19] C. Rino. (Sep. 30, 2010). *Satellite Orbit Computation*. [Online]. Available: <http://www.mathworks.com/matlabcentral/fileexchange/28888-satellite-orbit-computation>
- [20] X. Li, G. Liu, and J. Ni, "Autofocusing of ISAR images based on entropy minimization," *IEEE Trans. Aerosp. Electron. Syst.*, vol. 35, no. 4, pp. 1240–1252, Oct. 1999.
- [21] M. Martorella, F. Berizzi, and B. Haywood, "Contrast maximisation based technique for 2-D ISAR autofocusing," *IEE Proc. Radar, Sonar Navigat.*, vol. 152, no. 4, pp. 253–262, Aug. 2005.
- [22] M. Restano, R. Seu, and G. Picardi, "A phase-gradient-autofocus algorithm for the recovery of marsis subsurface data," *IEEE Geosci. Remote Sens. Lett.*, vol. 13, no. 6, pp. 806–810, Jun. 2016.
- [23] L. Zhao, L. Wang, G. Bi, and L. Yang, "An autofocus technique for high-resolution inverse synthetic aperture radar imagery," *IEEE Trans. Geosci. Remote Sens.*, vol. 52, no. 10, pp. 6392–6403, Oct. 2014.
- [24] O. Montenbruck and E. Gill, *Satellite Orbits: Models, Methods and Applications*. Boston, MA, USA: Springer, 2012.
- [25] Y. Zhang and Y. Zhong, "Calculation of subsatellite track of remote sensing satellite in nearly round orbit," *J. Inst. Surv. Mapping*, vol. 18, no. 4, pp. 257–269, 2001.
- [26] X. Ning, C. Ye, and J. Yang, "Radar aspect angle rate-of-change with respect to space target and its application," *J. Tsinghua Univ. (Sci. Technol.)*, vol. 53, no. 11, pp. 1558–1564, 2013.
- [27] Z. Bao, M. D. Xing, and T. Wang, *Radar Imaging Technology*. Beijing, China: Publishing House of Electronics Industry, 2005, pp. 24–40.
- [28] V. C. Chen and S. Qian, "Joint time-frequency transform for radar range-Doppler imaging," *IEEE Trans. Aerosp. Electron. Syst.*, vol. 34, no. 2, pp. 486–499, Apr. 1998.
- [29] X. Mao, J. Wang, and X. Liu, "ISAR minimum-entropy phase adjustment based on gradient descent algorithm," *Mod. Radar*, vol. 30, no. 1, pp. 40–43, 2008.
- [30] H. Darong, F. Cunqian, T. Ningning, and G. Yiduo, "2D spatial-variant phase errors compensation for ISAR imagery based on contrast maximisation," *Electron. Lett.*, vol. 52, no. 17, pp. 1480–1482, Aug. 2016.
- [31] F. Angel Garcia-Fernandez, A. Omar Yeste-Ojeda, and J. Grajal, "Facet model of moving targets for ISAR imaging and radar backscattering simulation," *IEEE Trans. Aerosp. Electron. Syst.*, vol. 46, no. 3, pp. 1455–1467, Jul. 2010.
- [32] F. Wang, T. F. Eibert, and Y. Q. Jin, "Simulation of ISAR imaging for a space target and reconstruction under sparse sampling via compressed sensing," *IEEE Trans. Geosci. Remote Sens.*, vol. 53, no. 6, pp. 3432–3441, Jun. 2015.
- [33] Y. Zhou, L. Zhang, H. Wang, Z. Qiao, and M. Hu, "Attitude estimation of space targets by extracting line features from ISAR image sequences," in *Proc. IEEE Int. Conf. Signal Process., Commun. Comput. (ICSPCC)*, Oct. 2017, pp. 1–4.
- [34] J. T. Mayhan, M. L. Burrows, K. M. Cuomo, and J. E. Piou, "High resolution 3D 'snapshot' ISAR imaging and feature extraction," *IEEE Trans. Aerosp. Electron. Syst.*, vol. 37, no. 2, pp. 630–642, Apr. 2001.
- [35] J. Nocedal and S. J. Wright, *Numerical Optimization*. Boston, MA, USA: Springer, 2006, pp. 192–202.
- [36] L. Ran, Z. Liu, L. Zhang, T. Li, and R. Xie, "An autofocus algorithm for estimating residual trajectory deviations in synthetic aperture radar," *IEEE Trans. Geosci. Remote Sens.*, vol. 55, no. 6, pp. 3408–3425, Jun. 2017.



**Yejian Zhou** was born in Taizhou, Zhejiang, China, in 1993. He received the B.S. degree in electronic engineering from Xidian University, Xi'an, China, in 2015, where he is currently pursuing the Ph.D. degree in signal processing with the National Laboratory of Radar Signal Processing.

His research interests include inverse synthetic aperture radar imaging and image interpretation.



**Lei Zhang** was born in Lishui, Zhejiang, China, in 1984. He received the Ph.D. degree from Xidian University, Xi'an, China, in 2012.

He is currently an Associate Professor with the National Laboratory of Radar Signal Processing, Xidian University, and also with the School of Electronics and Communication Engineering, Sun Yat-sen University, Guangzhou, China. His research interests include radar imaging [synthetic aperture radar (SAR)/inverse SAR] and motion compensation.



**Yunhe Cao** was born in Dangshan, Anhui, China. He received the B.S., M.S., and Ph.D. degrees from Xidian University, Xi'an, China, in 2001, 2004, and 2006, respectively.

He is currently a Professor with the National Laboratory of Radar Signal Processing, Xidian University. His research interests include multiple in multiple out radar, digital array radar, adaptive signal processing, and target detection.